catalysts

MDPI

Article

Synthesis and Experimental Screening of Catalysts for H_2S to H_2 Decomposition Under Close-to-Industry Conditions

Timur Palankoev [1,*], Anton Manakhov [1], Andrey Kovalskii [1], Ekaterina Sukhanova [2], Zakhar Popov [2,3], Dmitry Chareev [4], Konstantin Dement'ev [5], Anton Maximov [5] and Abdulaziz Al-Qasim [6]

1 Aramco Innovations LLC, 119234 Moscow, Russia; anton.manakhov@aramcoinnovations.com (A.M.)
2 Emanuel Institute of Biochemical Physics RAS, 119334 Moscow, Russia
3 Academic Department of Innovational Materials and Technologies Chemistry, Plekhanov Russian University of Economics, 117997 Moscow, Russia
4 Institute of Experimental Mineralogy (IEM RAS), 142432 Chernogolovka, Russia
5 Topchiev Institute of Petrochemical Synthesis RAS, 119991 Moscow, Russia; kdementev@ips.ac.ru (K.D.)
6 Research and Development Center, Saudi Aramco, Dhahran 34466, Saudi Arabia
* Correspondence: timur.palankoev@aramcoinnovations.com

Abstract: The chemical engineering community has shown significant interest in investigating methods to decompose hydrogen sulfide into hydrogen and sulfur. However, there is still a lack of detailed experimental data enabling us to choose the optimal catalyst, reaction, and regeneration conditions, as well as the overall process design. The purpose of this work is to synthesize a series of catalysts and compare their catalytic activity under the same conditions, chosen on the basis of a possible large-scale H_2S conversion process. To achieve this, the obtained catalysts were characterized by BET, XRD, SEM, TEM, and XPS before and after the reaction. Decomposition was conducted in a laboratory fixed-bed reactor at a temperature of 500 °C, 10 vol% of H_2S in the feed, and a GHSV of 540–1000 h^{-1}. DFT calculations evaluated the H_2S bond cleavage on various catalyst surfaces. It was shown that the most promising catalyst was Ni_3S_2, offering an acceptable H_2S conversion of 40%. We also observed that Ni_3S_2 catalyst regeneration could be conducted at much milder conditions compared to those previously reported in the literature. These results highlight the viability of upscaling the process with the selected catalyst.

Keywords: H_2S; hydrogen production; transition metal sulfides; hexaaluminates; sour gas treatment

Citation: Palankoev, T.; Manakhov, A.; Kovalskii, A.; Sukhanova, E.; Popov, Z.; Chareev, D.; Dement'ev, K.; Maximov, A.; Al-Qasim, A. Synthesis and Experimental Screening of Catalysts for H_2S to H_2 Decomposition Under Close-to-Industry Conditions. *Catalysts* **2024**, *14*, 839. https://doi.org/10.3390/catal14110839

Academic Editor: Guido Busca

Received: 7 October 2024
Revised: 8 November 2024
Accepted: 15 November 2024
Published: 20 November 2024

1. Introduction

Hydrogen sulfide gas is one of the byproducts of the oil industry, which can be present in natural gas ranging from trace amounts to tens of volume percent. H_2S is also produced by hydrotreating oil fractions up to 10 vol% in a circulating hydrogen stream and is concentrated in the acid gas during sour gas sweetening [1–3]. The Claus process has long been known and used as a method for the conversion of hydrogen sulfide to sulfur. It has been improved many times since its implementation to minimize harmful emissions and increase sulfur recovery, which nowadays can exceed 99% [4].

Alternative conversion methods enabling the conversion of H_2S into sulfur and valuable hydrogen also draw a lot of interest. Different approaches were suggested, such as plasma discharge [5,6], thermal and thermocatalytic conversion [7,8], or the use of microorganisms [9]. The latter is already commercially available technology [10]. Thermal decomposition is a straightforward and well-established method that involves the splitting of the H_2S molecule into hydrogen and sulfur through dissociation at elevated temperatures. However, even at temperatures as high as 1000 °C, a conversion of only 15% is possible due to the thermodynamic limitations of this reaction. By introducing catalysts, it is possible to lower the reaction temperature, hence lowering the energy consumption. To date, a considerable number of studies have been published concerning the decomposition

of hydrogen sulfide in the presence of metal sulfides (Mo-W [11–15], Fe-Co-Ni [12,15–21], Cu [16], etc. [22]), metal oxides [23–25], and oxygen-containing structures such as hexaaluminates, perovskites, and hydrotalcites [26–29]. Using the suggested catalysts, high hydrogen yield has been achieved within the considerably lower temperature range of 500–900 °C.

However, to proceed with the implementation of a thermocatalytic process for converting H_2S to H_2, there is a pressing need for organized experimental data on H_2S decomposition under close-to-industry reaction conditions. Today, transferring the reported results to the industry is still problematic. Numerous articles choose very low H_2S concentrations in the feed flow (around 1000 ppmv) or extremely high contact time. In practice, the H_2S concentration in sour gas streams can vary from 10 to 50 vol%, and the flow rate prevents the reaction from being conducted for hours. These results cannot be used to assess the technology. Furthermore, it is sometimes difficult to compare the results due to substantial variations in the experimental design and initial conditions. For example, some studies do not specify the parameters of the process, such as gas hourly space velocity (GHSV), contact time, or catalyst load, which could lead to severely different hydrogen yield in the presence of the same catalyst under seemingly the same conditions: temperature and H_2S initial concentration [11,12].

The purpose of this work is to synthesize the most promising (according to the literature) catalysts for hydrogen sulfide decomposition and compare their activity under the same conditions using one given reactor. Secondly, to generalize the routes of hydrogen sulfide conversion on these materials, the changes in catalyst composition were characterized after catalysis. Lastly, an effort was made to identify the main influencing factors affecting the process of upscaling. The activity of synthesized catalysts was assessed at a reaction temperature of 500 °C, an initial H_2S concentration of 10 vol%, and a GHSV of 1000 h^{-1}. The temperature of 500 °C is the minimum in the studied range of thermocatalytic conversion of hydrogen sulfide, and its choice is determined by minimizing energy consumption during the possible implementation of the process; an initial concentration of hydrogen sulfide of 10 vol% was chosen for reasons related to modeling a realistically possible flow of acid gas containing H_2S; GHSV of 1000 h^{-1} was selected from the range of typical values for catalytic plants involved in hydrogen sulfide processing [30–32].

2. Results and Discussion

2.1. Catalysts

In this work, several catalysts for the decomposition of hydrogen sulfide into hydrogen and sulfur were synthesized, namely the following:

- Series of FeS doped with Mo at a concentration of 1–3 at%;
- Series of FeS doped with W at a concentration of 1–3 at%;
- A sample of pyrrhotite-like structure doped with Mo: $(Fe_{0.98}Mo_{0.02})_{0.87}S$;
- A sample of pyrrhotite-like structure doped with W: $(Fe_{0.98}W_{0.02})_{0.87}S$;
- A sample of Ni_3S_2;
- Series of hexaaluminate catalysts: $LaFe_xAl_{12-x}O_{19}$, where x = 2, 4, or 6.

The methods for preparing these catalysts are provided separately in Section 3, and more detailed data are provided in the Supplementary Materials.

The structure and compositions of catalysts were analyzed and confirmed using TEM and XRD. According to micrographs (Figure 1), most samples consisted of particles with a size of 100–500 nm. Particles of the $Fe_{0.98}Mo_{0.02}S$ sample were somewhat larger in the range of 1–3 μm. The XRD spectra of sulfide catalysts are provided in Figures 2 and 3, while synthesized aluminate XRD spectra are summarized in Figure 4. Target phases were detected in all obtained samples, and the data were consistent with the literature [21,26] as all diffraction peaks were observed, which were attributed to (1) FeS with a distorted lattice due to doping; (2) rhombohedral Ni_3S_2; and (3) a magnetoplumbite phase, which is characteristic for reported hexaaluminate catalysts. A sole exception was the identified additional phase of MoS_2/WS_2 in some samples, the impact of which on the catalytic

activity will be discussed below. According to STEM elemental mapping, the distribution of metals over the surface of the particles is even (Figure 5).

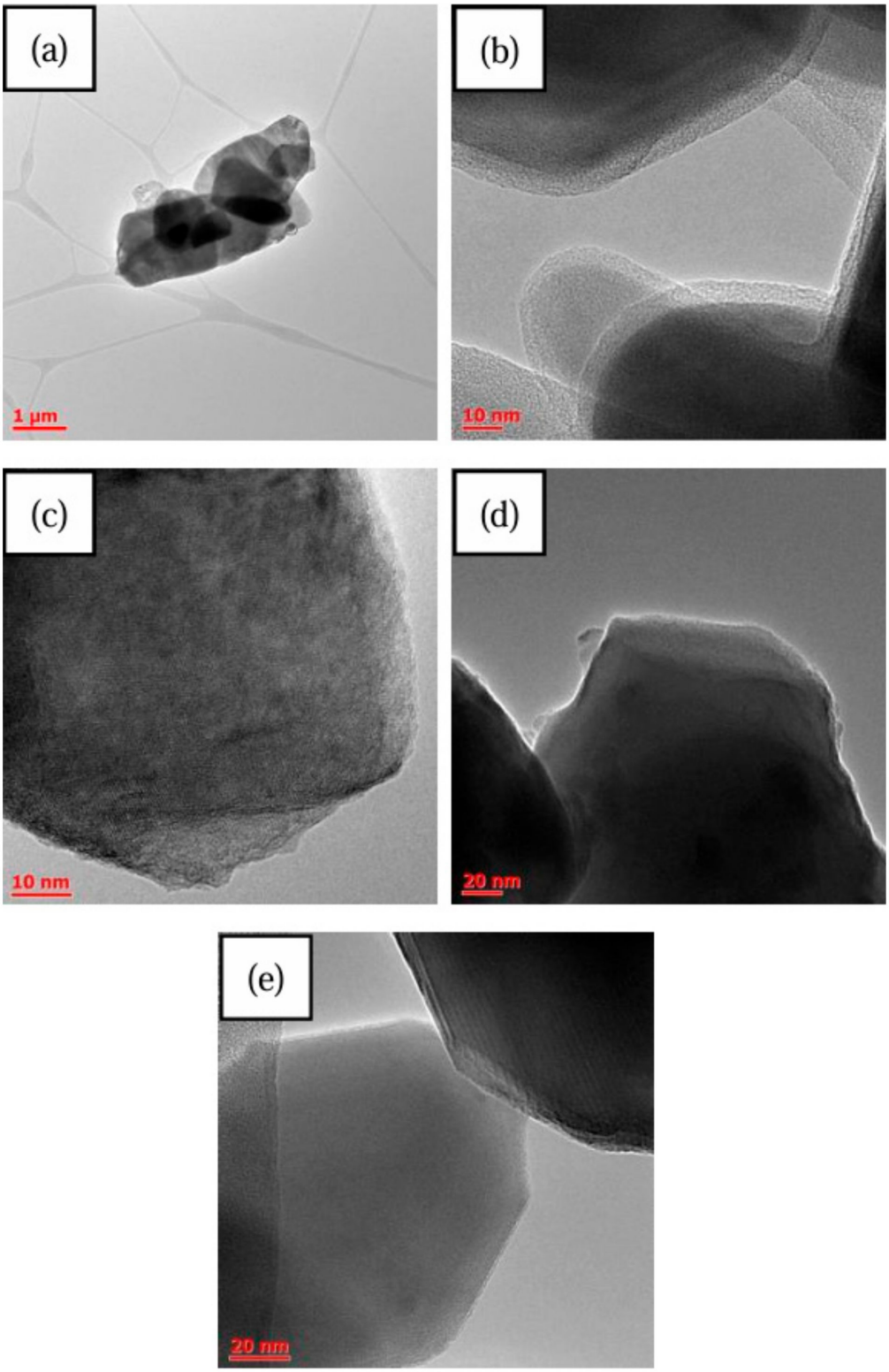

Figure 1. Typical micrographs of obtained catalysts: (**a**) $Fe_{1-x}Mo_xS$ troilite series; (**b**) $Fe_{1-x}W_xS$ series; (**c**) $(Fe_{0.98}Mo(W)_{0.02})_{0.87}S$ pyrrhotite-like series; (**d**) Ni_3S_2; and (**e**) $LaFe_xAl_{12-x}O_{19}$ hexaaluminate series.

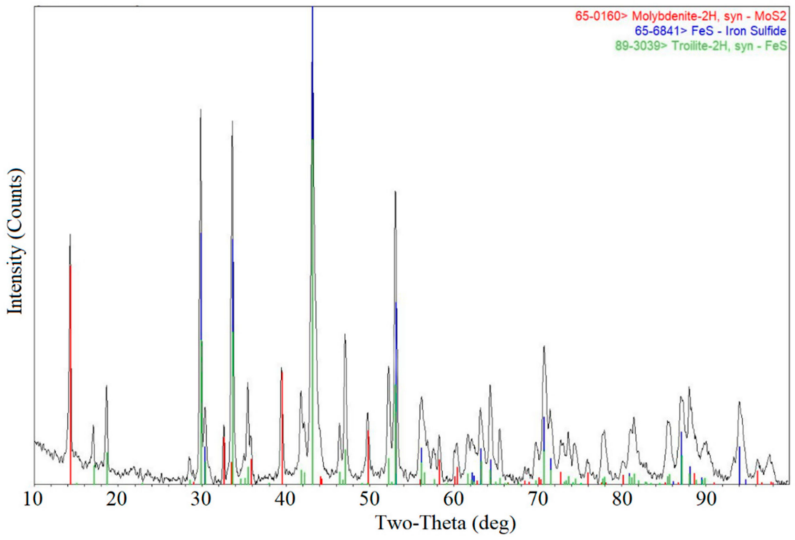

Figure 2. Typical XRD pattern of the troilite series catalysts $Fe_{(1-x)}Mo_xS$.

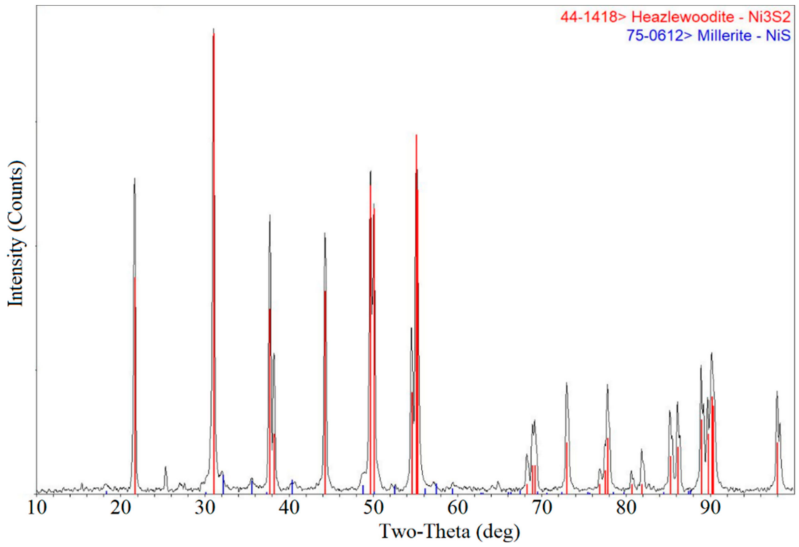

Figure 3. XRD pattern of the Ni_3S_2 sample.

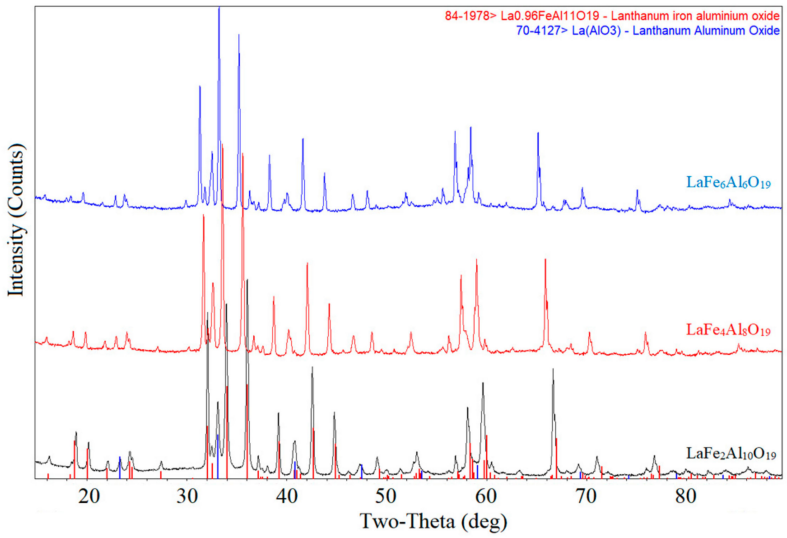

Figure 4. Typical XRD patterns of $LaFe_xAl_{(12-x)}O_{19}$ hexaaluminate series.

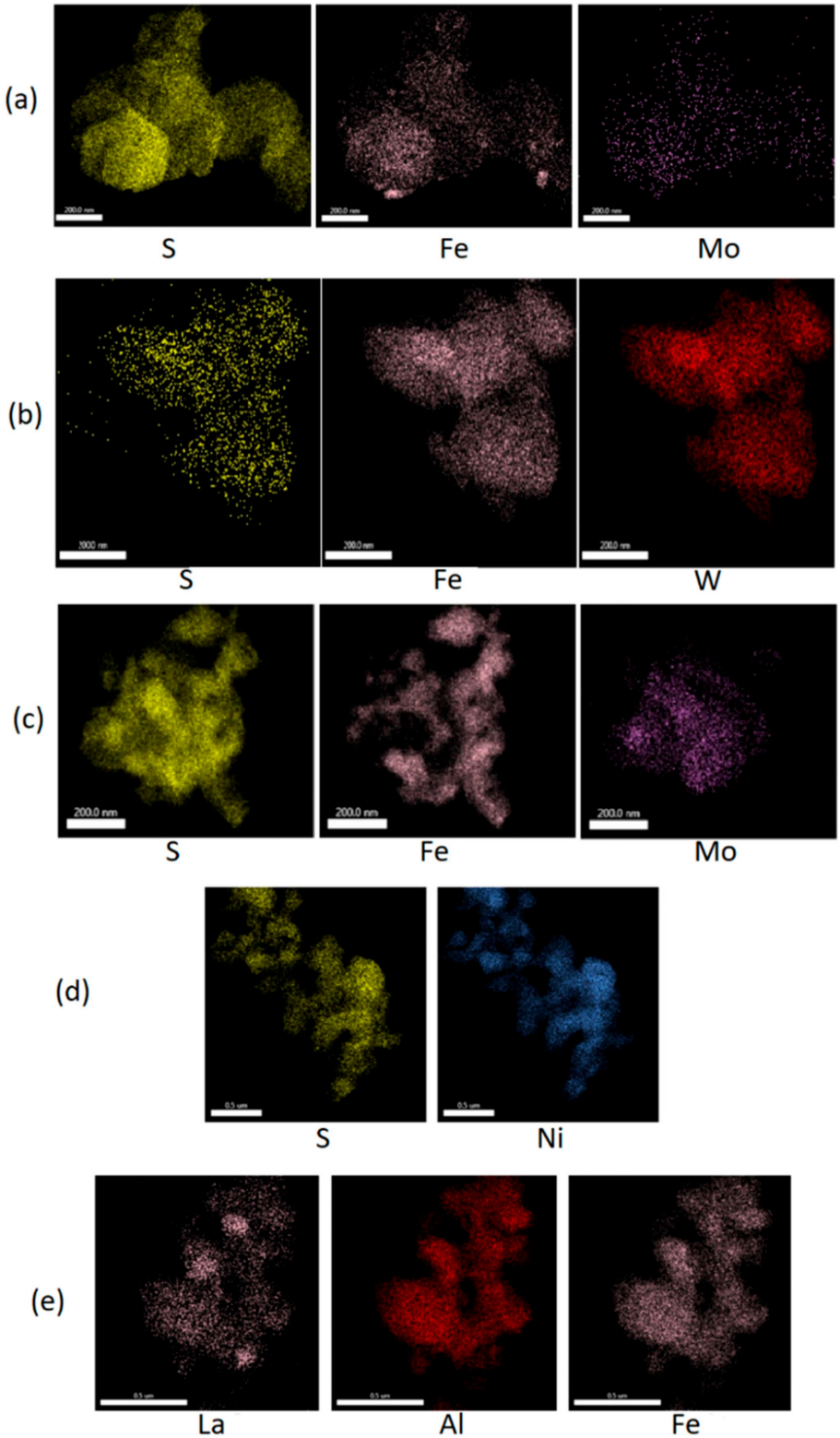

Figure 5. Typical elemental distribution maps for (**a**) $Fe_{(1-x)}Mo_xS$ troilite series; (**b**) $Fe_{(1-x)}W_xS$ series; (**c**) $(Fe_{0.98}Mo_{0.02})_{0.87}S$ pyrrhotite-like series; (**d**) Ni_3S_2; and (**e**) $LaFe_xAl_{(12-x)}O_{19}$ hexaaluminate series.

According to the adsorption isotherms obtained by BET analysis, the catalyst powder samples can be classified as non-porous. The estimated specific surface area of such samples lies in the range of 1–10 m^2/g. On the other hand, the synthesized supported Ni_3S_2/AAO is characterized by a high specific surface area of 251 m^2/g, with an initial characteristic of

291 m^2/g. The decrease in specific surface area is most likely due to the blocking of pores by active phase particles deposited on the surface.

2.2. Catalyst Activity Tests

The performance of doped troilite samples is illustrated in Figure 6. The observed impact of the dopant aligns with the existing body of knowledge: the addition of Mo as a dopant leads to an enhancement in hydrogen production, resulting in an increase in hydrogen yield from 8% to 10%. The optimal concentration of dopant is 2 atomic percent (at%). It should be noted that the W-doped FeS sample with the W concentration of 2 at% exhibits comparable activity in the decomposition of hydrogen sulfide. Based on DFT calculations, Jangam and co-workers came to the conclusion that the role of the dopant is mainly to facilitate the diffusion of hydrogen rather than affect the observed reaction energy barrier [21]. Apparently, the same effect can be achieved by introducing W atoms into the FeS catalyst. The relatively low hydrogen yield in the case of $Fe_{0.99}W_{0.01}S$ against the $Fe_{0.99}Mo_{0.01}S$ catalyst (6% hydrogen yield compared to 8%, respectively) is supposedly due to the phase separation for the W-doped sample. This was suspected after the XRD results demonstrated strong reflexes corresponding to the WS_2 phase. As mentioned before, an additional phase of MoS_2/WS_2 was identified in some troilite samples. However, in the case of $Fe_{0.99}W_{0.01}S$, such phase separation was stronger and possibly hindered its activity.

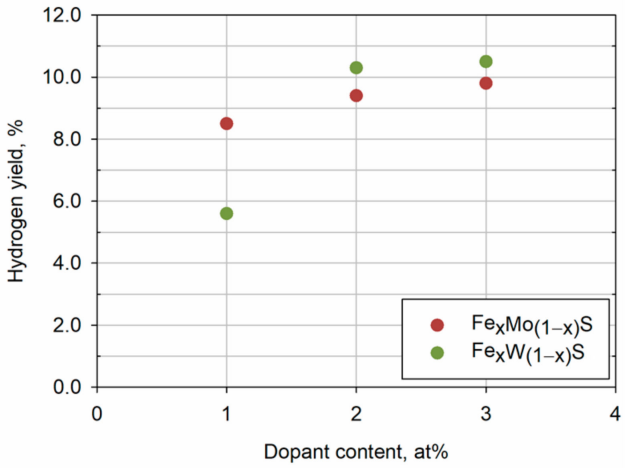

Figure 6. Dependence of hydrogen yield in the presence of troilite samples doped with different quantities of Mo or W. Reaction conditions: 500 °C, 10 vol% of H_2S in the feed, GHSV of 1000 h^{-1}.

A comparison of hydrogen yield obtained using pyrrhotite-like catalysts $(Mo_{0.02}Fe_{0.98})_{0.87}S$ and $(W_{0.02}Fe_{0.98})_{0.87}S$ with the corresponding troilite-like samples is shown in Figure 7. It can be concluded that sulfides with excess sulfur have low activity in the conversion of hydrogen sulfide to hydrogen. This result is consistent with the sulfur looping concept, according to which metal sulfides with a metal/sulfur ratio of less than 1 are considered deactivated and require the removal of sulfur. The decline in catalyst activity can also be attributed to a reduction in the reaction rate caused by the accumulation of sulfur on the catalyst's surface. This conclusion is indirectly confirmed by the results of the work of Kwok and others [13]. In their study, the researchers successfully obtained a hydrogen yield of 10% using a flow reactor and a core–shell catalyst consisting of a MoS_2 core encapsulated in a SiO_2 shell. The creation of that specific structure facilitated the diffusion of hydrogen sulfide and the elimination of reaction byproducts, resulting in a beneficial effect on the hydrogen yield. The difference in hydrogen yield for $(Mo_{0.02}Fe_{0.98})_{0.87}S$ and $(W_{0.02}Fe_{0.98})_{0.87}S$ was not considered in this work as a significant result since it is most likely associated with a large error in determining the hydrogen yield at such low conversion values.

The obtained hydrogen yield during the decomposition of H_2S in the presence of hexaaluminates is shown in Figure 8. The studied systems have low catalytic activity in the

decomposition of hydrogen sulfide under the studied conditions (500 °C, 1000 h^{-1}). The obtained hydrogen yield fluctuates around 1%, and its change for studied hexaaluminates is more likely due to experimental error than due to the influence of the Fe/Al ratio. In the literature, these materials were proposed in the work of Jiang and co-workers [26], where it was demonstrated that it was possible to achieve high conversion of hydrogen sulfide (above 50%) at a temperature of 800 °C. The authors proposed a path for direct dehydrogenation of hydrogen sulfide catalyzed by Fe^{3+} centers in the aluminate structure, which was also supported by DFT calculations.

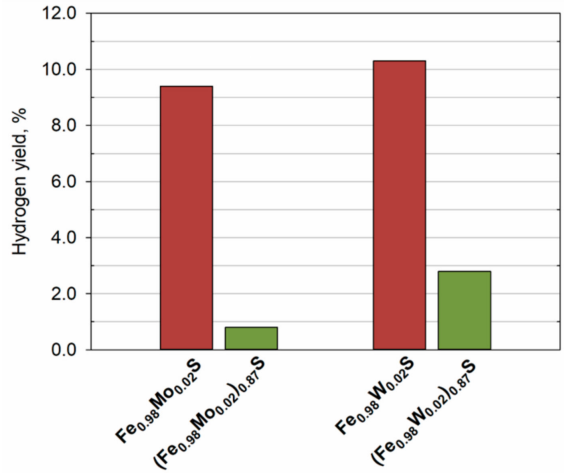

Figure 7. Comparison of the hydrogen yield obtained during H_2S decomposition in the presence of pyrrhotite-like and troilite-like catalysts. Reaction conditions: 500 °C, 10 vol% of H_2S in the feed, GHSV of 1000 h^{-1}.

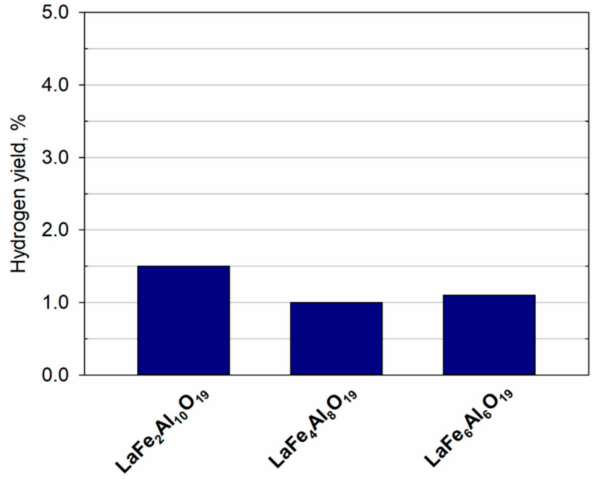

Figure 8. Comparison of the hydrogen yield obtained during H_2S decomposition in the presence of hexaaluminate catalysts. Reaction conditions: 500 °C, 10 vol% of H_2S in the feed, GHSV of 1000 h^{-1}.

After catalysis, the XRD spectra of hexaaluminate catalysts are essentially identical to those of the initially synthesized ones. All sulfide catalysts demonstrate the emergence of new phases: Fe_7S_8 for pyrrhotite-like and troilite-like catalysts and NiS for the N_3S_2 catalyst (Figures S1–S4 in the Supplementary Materials). This means that no sulfur was included in the structure of hexaaluminate catalysts during contact with H_2S. However, according to STEM elemental mapping, an accumulation of sulfur is observed on the surface of the aluminates (Figure 9), which apparently represents elemental sulfur formed during the decomposition of hydrogen sulfide during interaction with iron atoms in the structure of the aluminate, as suggested in the literature.

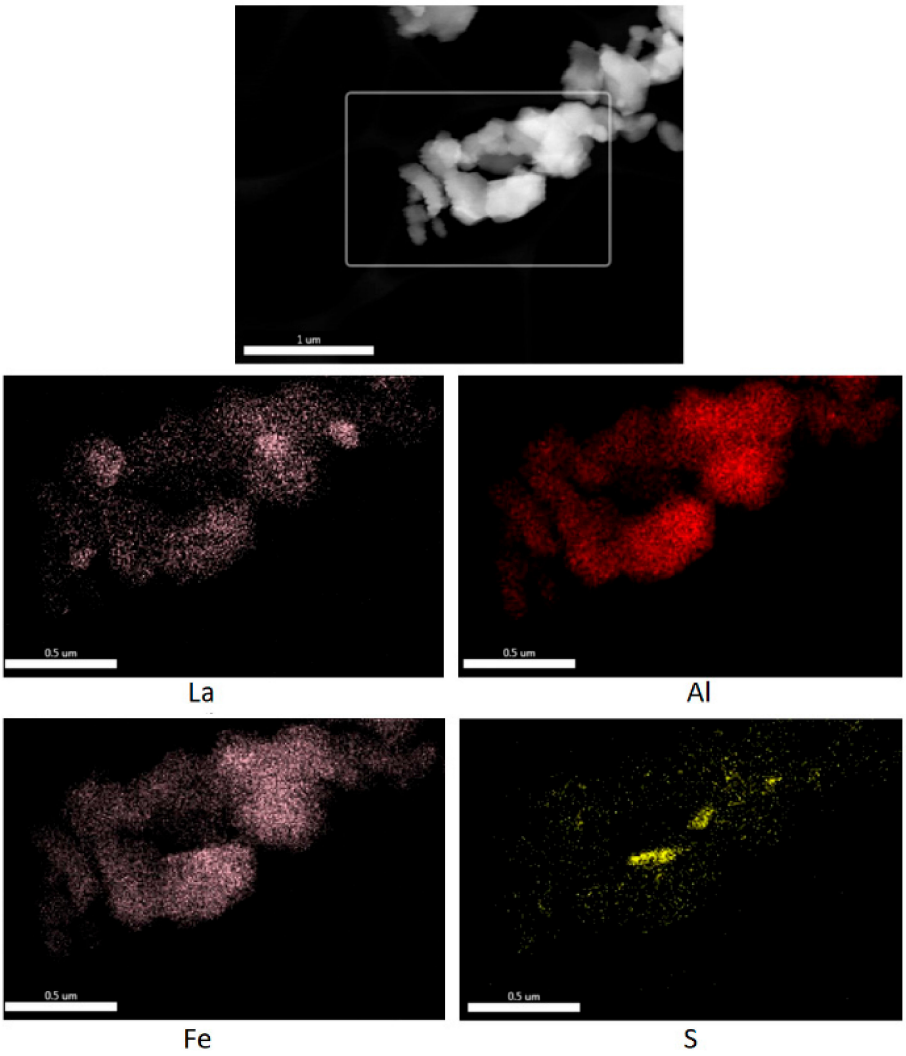

Figure 9. STEM elemental mapping on the surface of the $LaFe_4Al_{10}O_{19}$ sample after catalysis.

2.3. Catalyst Regeneration

The highest catalytic activity among the studied materials under the selected H_2S decomposition conditions (10 vol% H_2S, 500 °C, GHSV 1000 h^{-1}) is demonstrated by the Ni_3S_2 sample exhibiting a hydrogen yield of 23%. The activity of such sulfide is due to the sulfidation process yielding hydrogen and NiS phase. This was verified through X-ray diffraction (XRD), X-ray photoelectron spectroscopy (XPS), and scanning transmission electron microscopy (STEM) elemental mapping analysis. Please refer to Figures S4–S7 in the Supplementary Materials for further details. The Ni2p spectrum was fitted with a sum of three components: Ni^{3+} (BE = 856 eV), Ni-S satellite (BE = 861.6 eV), and Ni^{2+} (BE = 853 eV). The obtained XPS spectrum correlates with the published data, and a minor contribution of Ni^{2+} is often observed for Ni_3S_2 [33]. The S2p peak was fitted with three components, namely NiS (BE = 162.5 eV), NiS_2 (BE = 164 eV) and SO_4^{2-} (BE = 169.6 eV). The presence of sulfates might be related to surface oxidation also observed before [33]. In the "sulfur looping" process, the catalyst is heated in the presence of an inert gas. This results in the sulfur that builds up during the decomposition of hydrogen sulfide to be released from the crystal structure of the sulfide and evaporate from the surface. In the meantime, the sulfide phase responsible for breaking down hydrogen sulfide is regenerated. Moreover, within this study, it was found that the regeneration of the catalyst can be carried out at a temperature lower than proposed in the literature [17], which is confirmed by TGA data for the deactivated nickel catalyst powder. Indeed, the beginning of the transition of NiS to Ni_3S_2 with a mass loss close to 11.8% is observed already at a temperature of 600 °C.

The catalytic activity of the nickel catalyst after the thermal treatment at this temperature for an hour is restored almost completely (Figure 10). The difference in hydrogen yield for fresh and regenerated catalysts is negligible (23 vs. 22%) given the relative error in the analysis of the gaseous products (10% relative as stated in the Section 3).

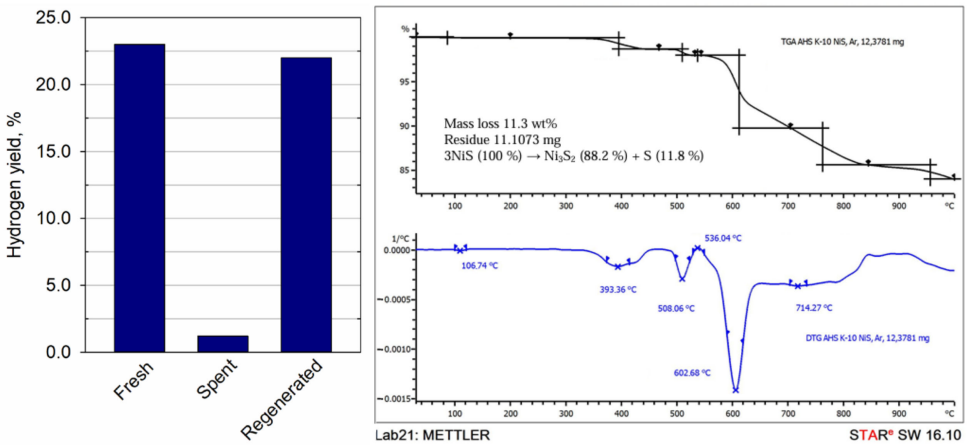

Figure 10. (**left**) Hydrogen yield obtained for H_2S decomposition on fresh, deactivated and regenerated Ni_3S_2; (**right**) TGA (black line) and DTG (blue line) curves of a NiS sample heated in a flow of inert gas.

2.4. Supported Catalyst Tests

Figure 11 presents a comparison of the activity of powder and supported catalysts for nickel-based systems. An increase in the hydrogen yield from 23 to 27% was noted, which can be explained by an increase in the dispersion of active phase particles and their stabilization by the Al_2O_3 matrix. Here, we also demonstrated that the distribution of Ni_3S_2 particles on the matrix has a beneficial effect on the catalyst, lowering its deactivation rate (Figure 12). The sudden loss of activity is attributed to near complete Ni_3S_2 sulfidation to NiS, which is supported by XRD analysis (Figure S4 in the Supplementary Materials). The latter phase is not active in H_2S conversion, and small quantities of Ni_3S_2 left are either inaccessible or cannot support adequate conversion due to the very high actual GHSV of H_2S per active catalyst left.

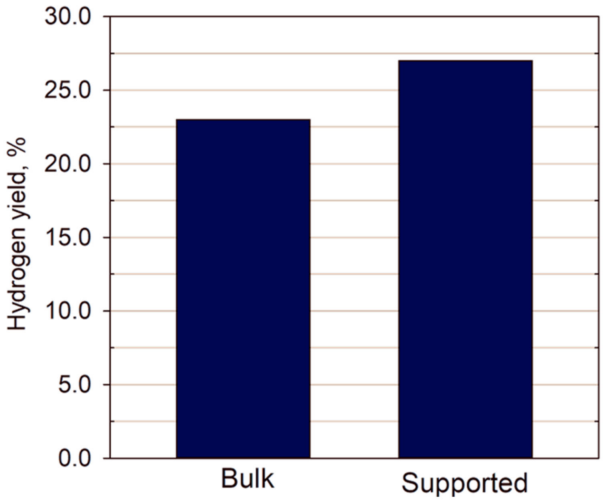

Figure 11. Comparison of hydrogen yield achieved on Ni_3S_2 powder and Al_2O_3 supported Ni_3S_2. Reaction conditions: 500 °C, 10 vol% of H_2S in the feed, GHSV of 1000 h^{-1}.

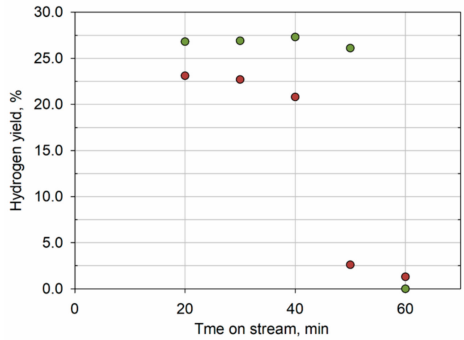

Figure 12. Change in hydrogen yield over time during decomposition of H_2S on Ni_3S_2 powder (red dots) and Al_2O_3 supported Ni_3S_2 (green dots). Reaction conditions: 500 °C, 10 vol% of H_2S in the feed, GHSV of 1000 h^{-1}.

The effect of GHSV on the yield of hydrogen during the decomposition of hydrogen sulfide in the presence of Ni_3S_2 is presented in Figure 13. With the decrease of GHSV to 540 h^{-1}, an increase in the hydrogen yield is observed by almost 1.5 times. The obtained result can be explained by the fact that a decrease in the GHSV means an increase in the contact time with the surface of Ni_3S_2, providing conditions for the diffusion of H_2S molecules to unreacted centers, their decomposition, and desorption of H_2. A further decrease in the GHSV did not lead to an additional increase in hydrogen yield, which apparently means that, in this case, it is already limited by the availability of fresh active sites, which decreases with the accumulation of sulfur on the catalyst surface.

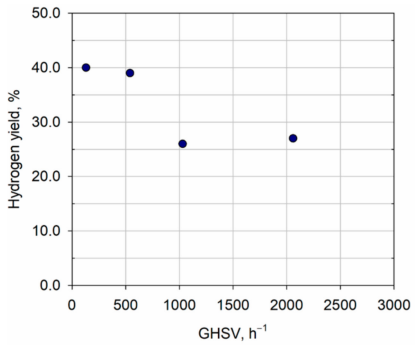

Figure 13. Hydrogen yield for H_2S decomposition in the presence of Ni_3S_2/AAO at 500 °C and different GHSV.

The comparison of the obtained results with the state of the art reported in the literature is presented in Table 1. As can be seen from the data, metal sulfides themselves possess quite low activity in H_2S decomposition. According to the reported DFT calculations, the reason for this is diffusion limitations [21]. Kwok et al. proposed a solution to this by synthesizing core-shell catalyst particles. However, in this work, we verified that doping sulfide is also a promising approach. The obtained doped catalyst gives a similar yield of hydrogen at a much higher initial H_2S concentration (10% versus 2500 ppm).

New data on H_2S decomposition to hydrogen in the presence of Ni_3S_2 were obtained in this work. We demonstrated that this material is highly active in hydrogen production from H_2S even at much lower temperatures and higher initial hydrogen sulfide concentrations than was reported before. These conditions simulate the more adequately possible conversion of H_2S in industry and could be used for evaluating hydrogen production on a larger scale, e.g., while designing a pilot plant.

In this work, for aluminates (described by $LaFe_xAl_{(12-x)}O_{19}$ formula), there is practically no catalytic activity that has been observed. We suppose that the main reason for such a low H_2 yield is the selected reaction temperature. Specifically, high H_2 yield was reported in the literature but at temperatures as high as 800 °C (Table 1, Ref. [26]). In this work, it

was demonstrated that at 500 °C, this catalyst is practically inactive in H_2S decomposition. However, further research is needed to study the temperature dependence of H_2 yield for this catalyst.

Table 1. Achieved hydrogen yield under different conditions of H_2S decomposition. Comparison of the results with recent publications.

Ref.	Catalyst	Temp., °C	GHSV, h^{-1}	H_2S Content, vol%	H_2 Yield, %
		Metal sulfides			
[12]	FeS	500	150 *	100	3
[13]	MoS_2 core SiO_2 shell	500	n/a	0.25	10
This work	$Fe_{0.98}Mo_{0.02}S$ $Fe_{0.98}W_{0.02}S$	500	1000	10	10
		Supported nickel sulfide			
[16]	Supported Ni	550	13,500	10	2.5
[17]	Supported Ni_3S_2	700	5000	0.9	80
This work	Supported Ni_3S_2	500	540	10	40
		Aluminates			
[26]	$LaFe_xAl_{(12-x)}O_{19}$	800	24,000	0.1	50
This work	$LaFe_xAl_{(12-x)}O_{19}$	500	1000	10	1

* Estimated by authors.

2.5. DFT Study

Jangam and co-authors [17] examined the effect of the surface area of the catalyst on the conversion of hydrogen sulfide, which is an important parameter in the general theory of heterogeneous catalysis. Unfortunately, in this article, the observed surface of Ni_3S_2 was limited to only S terminated (111) surface, while the ideal equilibrium morphology for Ni_2S_3 nanoparticles can contain both (111) and (11−1)-type faces, based on theoretical calculations [34]. In our investigation, we take into consideration other possible surfaces of the Ni_3S_2 crystal: (001), (11−1), (110), (1−10), (−111), (−210), and (111). The analysis of the surface energy (see SM DFT Section 1) reveals the favorable ones: (111)_S, (001) with unequal sides A and B, (11−1)_S, (110)_3, (−111), (1-10), and (−210); see Figure 14.

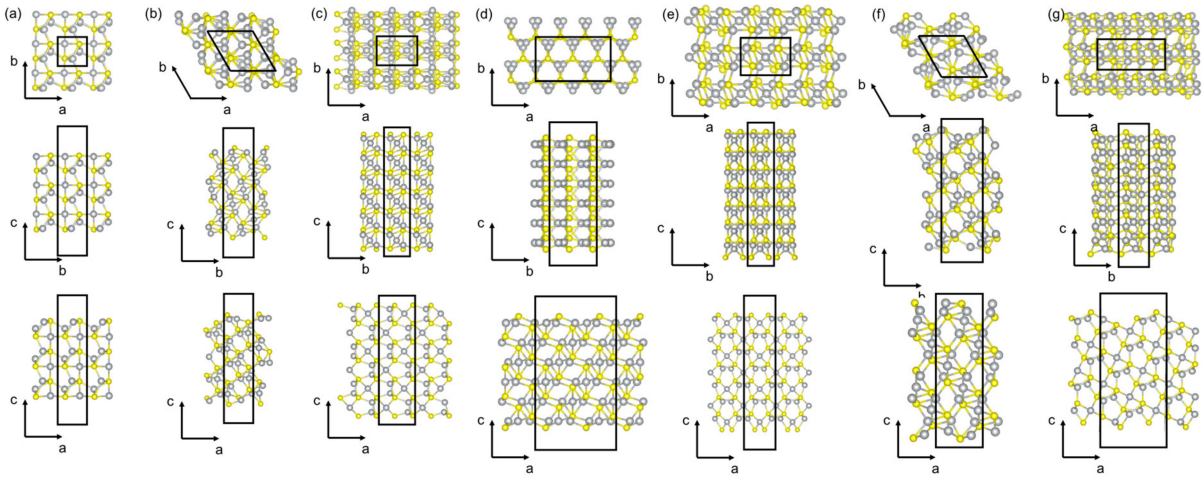

Figure 14. Considered surfaces of the Ni_3S_2 crystal: (**a**) (001) surface; (**b**) (11−1)_S surface terminated with sulfur atoms; (**c**) (110)_3 surface; (**d**) (111)_S surface terminated by sulfur atoms; (**e**) (1−10) surface terminated by sulfur atoms; (**f**) (−111) surface; and (**g**) (−210) surface. Gray and yellow colors indicate nickel and sulfur atoms, respectively. The surface unit cell (1 × 1) is indicated by black solid lines.

The barriers of individual stages of the hydrogen cleavage reaction from the hydrogen sulfide molecule on selected Ni_3S_2 crystal surfaces were calculated using the NEB method

in order to reveal the catalytic properties of these surfaces. The calculated values of the barriers are presented in Table 2.

Table 2. Barrier heights of individual stages of H_2S decomposition on Ni_3S_2 surfaces.

Surface	Barrier, (eV)	
	TS1	TS2
(111)_S	0.39	0.81
(001) side A	1.16	1.86
(001) side B	1.20	1.44
(11-1)_S	0.34	1.14
(110)_3	0.33	1.17
(−111)	1.01	0.97
(1-10)	1.24	0.57
(−210)	0.89	1.77

The transition state TS1 corresponds to reaction $H_2S^* \rightarrow HS^* + H^*$ and TS2 to $HS^* \rightarrow S^* + H^*$ reaction. The reaction paths were calculated between the most energetically favorable sorption positions of the H_2S molecule and its individual fragments (HS, S, H), which were determined before NEB calculations. Among all considered surfaces of Ni_3S_2, only three of them, (110)_3, (11-1)_S, and (111)_S, demonstrate a barrier less than 0.4 eV; at the same time, only (111) S surfaces show the lowest barrier for second hydrogen cleavage among these three with 0.81 eV barrier. Despite the 0.57 eV barrier for TS2 at (1-10) surface of Ni_3S_2, the reaction could be limited by the first stage with a 1.24 eV barrier.

3. Materials and Methods

For the synthesis of catalysts, FeS, MoS_2, WS_2 powders and Ni (II), La (III), Fe (III), Al (III) nitrates (all reagents ≥ 98 wt% pure, provided by LLC "ChemExpress"), and an $(NH_4)_2S$ solution (Sigma-Aldrich, 20 wt% aq. Solution, St. Louis, MO, USA) were used without further purification.

The synthesis of Fe sulfides doped with Mo and W was carried out using sintering of homogenized powders at a temperature of 850 °C for 48 h. The choice of FeS is justified by the fact that it is one of the potentially cheap and easily accessible compounds found in nature. Moreover, a theory has been proposed for the natural formation of hydrogen from H_2O molecules in the presence of Fe (II)-containing minerals, including FeS [35,36]. The crystallization of materials with the structure of both troilite (FeS) and pyrrhotite ($Fe_{0.87}S$) is possible in the Fe-S system [37]. The method of synthesis is described in detail elsewhere [38] and in the Supplementary Materials.

Nickel sulfide (Ni_3S_2) was synthesized according to the method proposed by Bezverkhyy and co-authors [39] by treating NiS with the flow of H_2-H_2S mixture at a temperature of 300 °C. This material was chosen as one of the promising catalysts for the "sulfur looping scheme" [40]. To evaluate the effect of the support, Ni_3S_2 supported on Al_2O_3 was synthesized. To obtain a supported catalyst, nickel was first distributed on Al_2O_3 by wet impregnation with $Ni(NO_3)_2$ and then converted to NiS by treating the catalyst with $(NH_4)_2S$. For more information, please refer to Supplementary Materials.

A series of hexaaluminate catalysts, $LaFe_xAl_{12-x}O_{19}$ (x = 2, 4, 6), were prepared using the carbonate route [26] via precipitating La, Fe, and Al nitrates solutions. A more detailed description of synthesis is given in the Supplementary Materials.

XRD analysis was carried out using a Rigaku X-ray spectrometer Rotaflex RU-200 using copper Kα radiation (λ = 0.154 nm) in 50 kV/160 mA mode in the angular range 2θ = 1–145° with a step of 0.04° and a shooting speed of 2 deg/min. Powdered samples (with a typical size of less than 10 μm) were used for analysis. Phase identification was carried out using the ICDD PDF-2 database.

SEM and TEM analysis were carried out using a FEI Tecnai G2 F20 S-TWIN TMP instrument with an EDAX EMF attachment and a holder for inertia-free heating DENS

Solutions A-SH30-4M-FS, accelerating voltage 200 kV. Powder samples were pre-dispersed in distilled water in an ultrasonic bath for 2 min, settled for 2–3 min, and then powder particles were deposited onto a copper mesh coated with a thin layer of amorphous carbon.

XPS spectra were obtained using a PHI VersaProbe II 5500 X-ray photoelectron spectrometer (primary X-ray photon energy 1100 eV, analysis depth up to 10 nm). Samples in powder form were placed on a thin layer of indium and pressed through glass to form a flat surface. To determine the elemental composition of the samples, the obtained XPS spectra were analyzed using specialized MultiPak 9.9.2 software.

The specific surface area (BET) of the catalysts was measured using a Belsorp instrument miniX with preliminary thermal degassing of the samples at a temperature of 300 °C and a pressure of 10 Pa for 10 h.

DTG analysis was carried out using Mettler Toledo Thermal Analysis System TGA/DSC 3+ while heating the sample at a rate of 10 °C/min in the flow of argon up to 1000 °C.

Catalytic tests were carried out in a tubular quartz reactor with a stationary catalyst bed at a temperature of 500 °C. 600 mg of catalyst was distributed in a layer of inert quartz beads to preserve a constant volume of the catalyst bed of 7 mL throughout the tests. The supported catalyst was loaded by weight without quartz beads so that the mass of the active phase was 600 mg. A hydrogen sulfide flow with an initial concentration of 10 vol% (balanced by N_2) was fed at a rate of 1000 h^{-1} (for this experimental setup, it corresponds to a feed flow rate of 3.6 l/h, with the estimated total volume of voids of 3.5 mL or 50% of the total volume).

Gaseous reaction products were collected for analysis by redirecting the gas flow at the outlet of the reactor into the chromatograph loop. Analysis of gaseous products was carried out using an LLC Meta-Chrome "Kristallux 4000M" chromatograph equipped with a capillary column HP-PLOT Q (15 m × 0.32 mm, stationary phase thickness 20 μm) and a thermal conductivity detector (TCD). Nitrogen was used as a carrier gas. The chromatograph was first calibrated using mixtures of H_2S-N_2 and H_2-N_2 mixtures. The average relative error in determining the hydrogen content is 10%. Hydrogen yield was calculated by the following equation:

$$Y = \frac{C(H_2)}{C(H_2S)} \times 100\%,$$

where $C(H_2)$ is the concentration of H_2 (vol%), and $C(H_2S)$ is the initial concentration of hydrogen sulfide (in this work 10 vol%).

The quantum–chemical calculations were carried out within the density functional theory (DFT) [41,42], implemented in the VASP package [43–45]. The exchange-correlation function was calculated in the generalized gradient approximation (GGA) in the Perdue–Burke–Ernzerhof (PBE) parameterization [46]. To describe the ion–electron interaction, the projector augmented wave method (PAW) [47] was used. Integration in the first Brillouin zone was performed using the Monkhorst–Pack method [48]. Relaxation of the atomic structure was carried out until the energy difference between the two steps of the ion optimization became less than 10^{-4} eV, and the energy difference between the two steps of the electron optimization cycle became less than 10^{-5} eV. In the calculations, Grimm dispersion corrections were applied to describe the van der Waals interaction (DFT-D3 method) [49]. The diffusion barriers were calculated using the nudged elastic band method (NEB) [50]. The VESTA [51] programs were used to visualize the atomic structure.

4. Conclusions

In this work, a number of catalysts were synthesized, and their catalytic activity was compared in the decomposition of H_2S to sulfur and hydrogen under the same conditions, chosen on the basis of modeling possible large-scale H_2S conversion process: temperature of 500 °C, H_2S initial concentration of 10 vol% and GHSV of 540–1000 h^{-1}. The obtained results were compared with the state of the art reported in the literature. It was demonstrated that under such conditions, the most promising catalyst is Ni_3S_2. This catalyst can

provide an acceptable H_2S conversion of 40% at concentrations as high as 10 vol% of H_2S in the feed. We also observed that Ni_3S_2 catalyst regeneration can be conducted at much milder conditions compared to previously reported in the literature. This contributes to the energy-effectiveness of the potential process. Obtained results contribute to the progress towards upscaling and implementing H_2S decomposition to H_2 and highlight the viable approach–thermocatalytic conversion in the presence of Ni_3S_2.

The DFT calculations reveal three surfaces of Ni_3S_2, (110)_3, (11−1)_S, and (111)_S, with the barrier of hydrogen cleavage from H_2S less than 0.4 eV at the first stage, which makes them most catalytic active, but only (111) S surfaces show the lowest barrier for hydrogen cleavage from HS among these three with an 0.81 eV barrier.

Supplementary Materials: The following supporting information can be downloaded at https://www.mdpi.com/article/10.3390/catal14110839/s1, Figure S1. Typical XRD pattern of the troilite series catalysts $Fe_{1-x}Mo_xS$ after catalysis; Figure S2. Typical XRD pattern of the troilite series catalysts $Fe_{1-x}W_xS$ after catalysis; Figure S3. XRD spectra comparison of $LaFe_xAl_{12-x}O_{19}$ hexaaluminate catalysts after catalysis; Figure S4. XRD spectra comparison for Ni_3S_2 original catalyst and after catalysis; Figure S5. XPS data on Ni_3S_2 catalyst before catalysis; Figure S6. XPS data on Ni_3S_2 catalyst after catalysis; Figure S7. STEM Elemental distribution maps for Ni_3S_2 after catalysis.

Author Contributions: Investigation, T.P., A.K., E.S., Z.P. and D.C.; data curation, A.M. (Anton Manakhov), K.D. and E.S.; writing—original draft preparation, T.P.; writing—review and editing, A.M. (Anton Manakhov), A.M. (Anton Maximov), A.K. and A.A.-Q.; conceptualization, A.A.-Q. All authors have read and agreed to the published version of the manuscript.

Funding: This research received no external funding.

Data Availability Statement: Data are contained within the article and Supplementary Material.

Acknowledgments: Authors Konstantin I. Dement'ev and Anton L. Maximov thank the Shared Research Center Analytical center of deep oil processing and petrochemistry of TIPS RAS for conducting XRD, BET, and TGA studies on the samples. The authors thank Rogacheva A.A. (junior researcher, TIPS RAS) for their help in conducting catalytic test runs.

Conflicts of Interest: Authors Timur Palankoev, Anton Manakhov, Andrey Kovalskii are employed by Aramco Innovations LLC. Authors declare no conflict of interest.

References

1. Pouliquen, F.; Blanc, C.; Arretz, E.; Labat, I.; Tournier-Lasserve, J.; Ladousse, A.; Nougayrede, J.; Savin, G.; Ivaldi, R.; Nicolas, M.; et al. Hydrogen Sulfide. In *Ullmann's Encyclopedia of Industrial Chemistry*; Wiley: New York, NY, USA, 2000. [CrossRef]
2. Bongartz, D.; Ghoniem, A.F. Impact of sour gas composition on ignition delay and burning velocity in air and oxy-fuel combustion. *Combust. Flame* **2015**, *162*, 2749–2757. [CrossRef]
3. Krenzke, D. Troubleshooting Hydrotreater Performance: Part I. A comprehensive review of operating parameters and performance issues affecting ULSD hydrotreater. *Refin. Oper.* **2011**, *2*, 1–11.
4. Khairulin, S.; Kerzhentsev, M.; Salnikov, A.; Ismagilov, Z.R. Direct Selective Oxidation of Hydrogen Sulfide: Laboratory, Pilot and Industrial Tests. *Catalysts* **2021**, *11*, 1109. [CrossRef]
5. Startsev, A.N. The crucial role of catalysts in the reaction of low temperature decomposition of hydrogen sulfide: Non-equilibrium thermodynamics of the irreversible process in an open system. *J. Mol. Catal.* **2020**, *497*, 111240. [CrossRef]
6. Li, J.; Chen, C.-B.; Wang, D.-D.; Li, C.-X.; Zhang, F.; Li, D.-B.; Min, D.; Li, W.-W.; Lam, P.K.S.; Yu, H.-Q. Solar-Driven Synchronous Photoelectrochemical Sulfur Recovery and Pollutant Degradation. *ACS Sustain. Chem. Eng.* **2018**, *6*, 9591–9595. [CrossRef]
7. De Crisci, A.G.; Moniri, A.; Xu, Y. Hydrogen from hydrogen sulfide: Towards a more sustainable hydrogen economy. *Int. J. Hydrogen Energy* **2019**, *44*, 1299–1327. [CrossRef]
8. Jangam, K.; Chen, Y.Y.; Qin, L.; Fan, L.S. Perspectives on reactive separation and removal of hydrogen sulfide. *Chem. Eng. Sci.* **2021**, *11*, 100105. [CrossRef]
9. Chan, Y.H.; Loy, A.C.M.; Cheah, K.W.; Chai, S.Y.W.; Ngu, L.H.; How, B.S.; Li, C.; Lock, S.S.M.; Wong, M.K.; Yiin, C.L.; et al. Hydrogen sulfide (H_2S) conversion to hydrogen (H_2) and value-added chemicals: Progress, challenges and outlook. *Chem. Eng. J.* **2023**, *458*, 141398. [CrossRef]
10. Paqell Home Page. Available online: https://Paqell.Com/ (accessed on 2 February 2024).
11. Fukuda, K.; Dokiya, M.; Kameyama, T.; Kotera, Y. Catalytic Decomposition of Hydrogen Sulfide. *Ind. Eng. Chem. Fundam.* **1978**, *17*, 243–248. [CrossRef]

12. Chivers, T.; Hyne, J.B.; Lau, C. The thermal decomposition of hydrogen sulfide over transition metal sulfides. *Int. J. Hydrogen Energy* **1980**, *3*, 499–506. [CrossRef]
13. Kwok, K.M.; Ong, S.W.D.; Chen, L.; Zeng, H.C. Constrained Growth of MoS_2 Nanosheets within a Mesoporous Silica Shell and Its Effects on Defect Sites and Catalyst Stability for H_2S Decomposition. *ACS Catal.* **2018**, *8*, 714–724. [CrossRef]
14. Wang, B.; Zhang, S.Y.; Ye, L.H.; Zhang, X.F.; Zhang, Y.F.; Chen, W.J. Exploring the Reaction Mechanism of H_2S Decomposition with MS_3 (M = Mo, W) Clusters. *ACS Omega* **2020**, *5*, 13324–13332. [CrossRef]
15. Jiang, G.; Yang, Z.; Zhang, F.; Li, G.; Wei, Z.; Niu, B.; Zhao, M.; Zhang, Z.; Hao, Z. Thermal Decomposition of H_2S at Low Temperature on Mo-Containing Catalysts Derived from MAlO (M = Mg, Co, and Ni) Layered Double Hydroxides. *Ind. Eng. Chem. Res.* **2023**, *62*, 7224–7234. [CrossRef]
16. Kraia, T.; Kaklidis, N.; Konsolakis, M.; Marnellos, G.E. Hydrogen production by H_2S decomposition over ceria supported transition metal (Co, Ni, Fe and Cu) catalysts. *Int. J. Hydrogen Energy* **2019**, *44*, 9753–9762. [CrossRef]
17. Jangam, K.V.; Joshi, A.S.; Chen, Y.Y.; Mahalingam, S.; Sunny, A.A.; Fan, L.S. Synergistic decomposition of H_2S into H_2 by Ni_3S_2 over ZrO_2 support via a sulfur looping scheme with CO_2 enabled carrier regeneration. *Chem. Eng. J.* **2021**, *426*, 131815. [CrossRef]
18. Kiucht, H.; Nakamura, T.; Funaki, K.; Tanaka, T. Recovery of hydrogen from hydrogen sulfide with metals or metal sulfides. *Int. J. Hydrogen Energy* **1982**, *7*, 477–482. [CrossRef]
19. Kiuchi, H.; Funaki, K.; Tanaka, T. Thermochemical decomposition of hydrogen sulfide with nickel sulfide. *Metall. Mater. Trans. B* **1983**, *14*, 347–352. [CrossRef]
20. Kraia, T.; Varvoutis, G.; MArnellos, G.E. Unveiling the Role of In Situ Sulfidation and H_2O Excess on H_2S Decomposition to Carbon-Free H_2 over Cobalt/Ceria Catalysts. *Catalysts* **2023**, *13*, 504. [CrossRef]
21. Jangam, K.; Chen, Y.Y.; Qin, L.; Fan, L.S. Mo-Doped FeS Mediated H_2 Production from H_2S via an in Situ Cyclic Sulfur Looping Scheme. *ACS Sustain. Chem. Eng.* **2021**, *9*, 11204–11211. [CrossRef]
22. Aljama, H.; Alaithan, Z.; Almofleh, A. Catalytic Conversion of H_2S to H_2: Challenges and Catalyst Limitations. *J. Phys. Chem. C* **2023**, *127*, 9022–9029. [CrossRef]
23. Palma, V.; Vaiano, V.; Barba, D.; Colozzi, M.; Palo, E.; Barbato, L.; Cortese, S. Oxidative Decomposition of H_2S over Alumina-Based Catalyst. *Ind. Eng. Chem. Res.* **2017**, *56*, 9072–9078. [CrossRef]
24. Reshetenko, T.V.; Khairulin, S.R.; Ismagilov, Z.R.; Kuznetsov, V.V. Study of the reaction of high-temperature H_2S decomposition on metal oxides (-Al_2O_3;-Fe_2O_3; V_2O_5). *Int. J. Hydrogen Energy* **2002**, *27*, 387–394. [CrossRef]
25. Sánchez-Hervás, J.; Ortiz, I.; Martí, V.; Andray, A. Removal of Organic Sulfur Pollutants from Gasification Gases at Intermediate Temperature by Means of a Zinc–Nickel-Oxide Sorbent for Integration in Biofuel Production. *Catalysts* **2023**, *13*, 1089. [CrossRef]
26. Jiang, G.; Zhang, X.; Zhang, F.; Liu, Z.; Wang, Z.; Hao, Z.; Lin, C. Efficient recovery of hydrogen and sulfur resources over non-sulfide based $LaFe_xAl_{12-x}O_{19}$ hexaaluminate catalysts by H_2S catalytic decomposition. *Appl. Catal. B* **2020**, *263*, 118354. [CrossRef]
27. Guldal, N.O.; Figen, H.E.; Baykara, S.Z. New catalysts for hydrogen production from H_2S: Preliminary results. *Int. J. Hydrogen Energy* **2015**, *40*, 7452–7458. [CrossRef]
28. Guldal, N.O.; Figen, H.E.; Baykara, S.Z. Perovskite catalysts for hydrogen production from hydrogen sulfide. *Int. J. Hydrogen Energy* **2018**, *43*, 1038–1046. [CrossRef]
29. Burra, K.R.G.; Bassioni, G.; Gupta, A.K. Catalytic transformation of H_2S for H_2 production. *Int. J. Hydrogen Energy* **2018**, *43*, 22852–22860. [CrossRef]
30. Chou, C.-L. H_2S/SO_2 removal in the modified-claus reaction over packed alumina beds. *Environ. Prog. Sustain. Energy* **1987**, *6*, 183–189. [CrossRef]
31. ZareNezhad, B. An investigation on the most important influencing parameters regarding the selection of the proper catalysts for Claus SRU converters. *J. Ind. Eng. Chem.* **2009**, *15*, 143–147. [CrossRef]
32. Sadighi, S.; Mohaddecy, S.R.S.; Rashidzadeh, M.; Nouriasl, P. Kinetic-based Models for Alumina and Titania Claus Catalysts Based on Experimental Data. *Pet. Chem.* **2020**, *60*, 321–328. [CrossRef]
33. Su, H.; Song, S.; Li, S.; Gao, Y.; Ge, L.; Song, W.; Ma, T.; Liu, J. High-valent bimetal Ni_3S_2/Co_3S_4 induced by Cu doping for bifunctional electrocatalytic water splitting. *Appl. Catal. B* **2021**, *293*, 120225. [CrossRef]
34. Aray, Y.; Vega, D.; Rodriguez, J.; Vidal, A.B.; Grillo, M.E.; Coll, S. First-Principles Study of Low Miller Index Ni_3S_2 Surfaces in Hydrotreating Conditions. *J. Phys. Chem. B* **2009**, *113*, 3058–3070. [CrossRef]
35. Wang, L.; Jin, Z.; Chen, X.; Su, Y.; Huang, X. The Origin and Occurrence of Natural Hydrogen. *Energies* **2023**, *16*, 2400. [CrossRef]
36. Liu, J.; Liu, Q.; Xu, H.; Ding, Q.; Zhu, D.; Meng, Q. Genesis and energy significance of natural hydrogen. *Unconv. Resour.* **2023**, *3*, 176–182. [CrossRef]
37. Grønvold, F.; Haraldsen, H.; Faurholt, C. On the Phase Relations of Synthetic and Natural Pyrrhotites (Fe(1-x)S). *Acta Chem. Scand.* **1952**, *6*, 1452–1469. [CrossRef]
38. Vaughan, D.J. *Mineral Chemistry of Metal Sulfides*; Earth Sciences: Cambridge, UK, 1978.
39. Bezverkhyy, I.; Danot, M.; Afanasiev, P. New low-temperature preparations of some simple and mixed Co and Ni dispersed sulfides and their chemical behavior in reducing atmosphere. *Inorg. Chem.* **2003**, *42*, 1764–1768. [CrossRef]
40. Osasuyi, O.; Quang, D.V.; Basina, G.; Al Wahedi, Y.; Abu Zahra, M.R.M.; Palmisano, G.; Al-Ali, K. Reversible Metal Sulfide Transition in a Two-Step Thermochemical H_2S Splitting. *Ind. Eng. Chem. Res.* **2022**, *61*, 6135–6145. [CrossRef]
41. Hohenberg, P.; Kohn, W. Inhomogeneous Electron Gas. *Phys. Rev.* **1964**, *136*, B864–B871. [CrossRef]

42. Kohn, W.; Sham, L.J. Self-Consistent Equations Including Exchange and Correlation Effects. *Phys. Rev.* **1965**, *140*, A1133–A1138. [CrossRef]
43. Kresse, G.; Furthmüller, J. Efficient iterative schemes for ab initio total-energy calculations using a plane-wave basis set. *Phys. Rev. B* **1996**, *54*, 11169–11186. [CrossRef]
44. Kresse, G.; Furthmüller, J. Efficiency of ab-initio total energy calculations for metals and semiconductors using a plane-wave basis set. *Comput. Mater. Sci.* **1996**, *6*, 15–50. [CrossRef]
45. Kresse, G.; Hafner, J. Ab initio molecular-dynamics simulation of the liquid-metal–amorphous-semiconductor transition in germanium. *Phys. Rev. B* **1994**, *49*, 14251–14269. [CrossRef] [PubMed]
46. Perdew, J.P.; Burke, K.; Ernzerhof, M. Generalized Gradient Approximation Made Simple. *Phys. Rev. Lett.* **1996**, *77*, 3865–3868. [CrossRef] [PubMed]
47. Blöchl, P.E. Projector augmented-wave method. *Phys. Rev. B* **1994**, *50*, 17953–17979. [CrossRef]
48. Monkhorst, H.J.; Pack, J.D. Special points for Brillouin-zone integrations. *Phys. Rev. B* **1976**, *13*, 5188–5192. [CrossRef]
49. Grimme, S. Accurate description of van der Waals complexes by density functional theory including empirical corrections. *J. Comput. Chem.* **2004**, *25*, 1463–1473. [CrossRef]
50. Henkelman, G.; Uberuaga, B.P.; Jónsson, H. A climbing image nudged elastic band method for finding saddle points and minimum energy paths. *J. Chem. Phys.* **2000**, *113*, 9901–9904. [CrossRef]
51. Momma, K.; Izumi, F. VESTA 3 for three-dimensional visualization of crystal, volumetric and morphology data. *J. Appl. Cryst.* **2011**, *44*, 1272–1276. [CrossRef]